

Nonlinear Methods for Shape Optimization Problems in Liquid Crystal Tactoids

J. H. Adler^a, A. S. Andrei^{a,*}, T. J. Atherton^b

^a*Department of Mathematics, Tufts University, Medford, MA 02155*

^b*Department of Physics and Astronomy, Tufts University, Medford, MA 02155*

Abstract

Anisotropic fluids, such as nematic liquid crystals, can form non-spherical equilibrium shapes known as tactoids. Predicting the shape of these structures as a function of material parameters is challenging and paradigmatic of a broader class of problems that combine shape and order. Here, we consider a discrete shape optimization approach with finite elements to find the configuration of two-dimensional and three-dimensional tactoids using the Landau de Gennes framework and a Q-tensor representation. Efficient solution of the resulting constrained energy minimization problem is achieved using a quasi-Newton and nested iteration algorithm. Numerical validation is performed with benchmark solutions and compared against experimental data and earlier work. We explore physically motivated subproblems, whereby the shape and order are separately held fixed, respectively, to explore the role of both and examine material parameter dependence of the convergence. Nested iteration significantly improves both the computational cost and convergence of numerical solutions of these highly deformable materials.

Keywords: Tactoids; shape optimization; quasi-Newton's method; nested iteration, nematic liquid crystals

2000 MSC: 76A15, 49M15, 65N30, 65N22, 65N55, 65K10

*Corresponding author

Email addresses: James.Adler@tufts.edu (J. H. Adler), Anca.Andrei@tufts.edu (A. S. Andrei), Timothy.Atherton@tufts.edu (T. J. Atherton)

1. Introduction

Liquid crystals (LCs) are intermediate phases of matter that exhibit long-range order like a crystal but retain fluid properties [1]. The *nematic* LC phase, in particular, lacks translational order but possesses orientational order characterized by a locally-preferred axis of molecular or particulate alignment; this direction may vary spatially at the cost of elastic energy. Due to the presence of orientational order, nematic liquid crystals possess anisotropic physical properties, such as surface tension, dielectric response, and elasticity. In contrast to an isotropic fluid, which only exhibits surface tension and no elastic effects, LCs may form non-spherical droplets known as *tactoids* [2] when suspended in a surrounding host isotropic fluid. Tactoids can assume various shapes and director field configurations depending on their size [2], elastic properties, and anisotropic surface tension strength [3]. Due to their potential to change shape and ability to conform to complex geometries [4, 5], tactoids are an exciting geometry for emerging technologies [6]. This includes enhancing LC displays' performance [7], serving as carriers for pharmaceuticals [8, 9], and developing materials with adaptive stiffness as seen in soft robots [10, 11, 12].

In this paper, we develop efficient and robust numerical methods based on nonlinear optimization techniques to predict the solution to tactoid shape-order problems. Using this approach, we compare our results with earlier work, Bates [13] and Prinsen and van der Schoot [2], all while improving upon previous research on modeling tactoids' various morphologies.

Numerical efforts to investigate the configuration of a nematic tactoid droplet have received extensive attention. Monte Carlo simulations have shown that a tactoid's aspect ratio can be temperature dependent [14] and that their morphologies can depend on the LC's orientational ordering [15]. For instance, various tactoid formations are determined by competition between the bending and surface tension energies as LCs exhibit phase transitions [16]. Monte Carlo methods have also been used to model tactoid defects [4, 17, 5]. While Monte Carlo methods are versatile, they are computationally expensive and require many simplifying assumptions on the model to achieve convergence. Phase field methods use an auxiliary scalar field to interpolate between the interior and exterior of a shape and have been used for modeling tactoids [17]. Such methods are powerful, but challenges arise when dealing with cusps in the manifold [18]. Level set methods, which represent the free boundary of the system as a contour or a level set of a scalar

function defined in a higher-dimensional space, have been used to model interfaces of tactoids and depict their defects [19]. While level set methods can model materials that change shape and topology, they require sophisticated numerical techniques, and including constraints can be challenging [20].

In contrast, finite-element discretizations with gradient descent (GD) based algorithms have been designed to iteratively adjust the position and orientational degrees of freedom in the tactoid to find stable nematic tactoid solutions under different conditions [21, 22]. DeBenedictis *et al.* [23] use a director formulation and Frank-Oseen energy to develop an alternating optimization scheme that takes GD iterations to solve for the director configuration, then solves for the optimal shape and repeats until convergence. While GD methods are computationally cheap per iteration using gradient-only calculations and are easy to implement, they possess linear convergence and hence need a high number of iterations to converge.

This paper aims to improve upon [23] by developing an integrated optimization method that simultaneously determines the shape and director configuration while ensuring physical validity. Predicting the optimal shape and physical fields involves solving a nonlinearly constrained optimization problem where we minimize the sum of bulk terms defined on a manifold, \mathcal{M} , and surface terms defined on the boundary $\partial\mathcal{M}$ while satisfying a nonlinear volumetric or surface area constraint. To expedite convergence, we use Newton’s method with Lagrange multipliers [24, 25], which offers local quadratic convergence and fewer iterations for faster solutions. However, Newton’s method requires calculation of the Hessian matrix of all functionals concerning shape and field and is sensitive to initial guesses, potentially hindering convergence to the correct solution. To mitigate computational expense, we approximate the Hessian using the well-established BFGS quasi-Newton method, sacrificing quadratic for local superlinear convergence. The method is implemented and run for physically-relevant parameters, reproducing several expected physical phenomena. We use nested iteration and Newton damping with line search [26, 25] to handle relatively poor initial guesses for efficient iterative convergence. Nested iteration techniques are a hierarchical approach to solving complex numerical problems, where coarse-grid solutions are used to accelerate convergence on finer grids, improving computational efficiency [27, 28, 29]. Nested iteration has been successfully applied to a variety of problems, including LC optimization problems [30]. Here, we demonstrate its efficiency in resolving the above-mentioned tactoid shapes.

Finally, we note that a great amount of work has been done on solution methods for solving LC problems in fixed boundaries. This includes deflation and parameter continuation for finding multiple stable LC configurations [31, 32, 33, 34] and multigrid preconditioners for the resulting linear systems [35, 36, 37, 38] to improve performance. As our focus is on the non-linear methods with nested iteration, we use direct solvers when needed and consider multigrid methods as future work.

The remainder of the paper is organized as follows. We first pose the shape optimization problem and construct its discrete version in Section 2. In Section 3, we derive the GD method from [23], the all-in-one quasi-Newton-based method, and describe the nested iteration approach used to improve computational efficiency in finding the optimal tactoid shape. Numerical experiments are reported in Section 4. Together with the full problem, we study two physically motivated subproblems, whereby either the shape or liquid crystal itself is held fixed, to understand the role of each better. We also study the formation of three-dimensional nematic tactoids and explain their similarities and differences to the two-dimensional case. We give concluding remarks in Section 5 and consider opportunities for future work.

2. Q-tensor Model for Tactoids

The configuration of a nematic liquid crystal is described by a vector or tensor field that encodes information about the local orientational ordering of the constituent molecules or particles. Several choices of representation are commonly used. The first possibility is to represent the local average molecular orientation by a unit vector field known as the *director*, \mathbf{n} . The director fully describes the nematic in the absence of *disclinations*, special points where \mathbf{n} is not uniquely defined and $\nabla\mathbf{n}$ diverges. If the director formulation is used, \mathbf{n} is a minimizer of the Frank-Oseen free energy model [39, 24] subject to the constraint that $\mathbf{n} \cdot \mathbf{n} = 1$ everywhere.

An alternative formulation, known as the Q-tensor approach [40, 1], encodes both orientational information as well as the local degree of alignment, denoted by a scalar field S , into a single tensor order parameter. In d -dimensions, and assuming that the alignment is uniaxial, the Q-tensor has the form,

$$\mathcal{Q} = S \left(\mathbf{n} \otimes \mathbf{n} - \frac{\mathcal{I}}{d} \right), \quad (1)$$

where \mathcal{I} is the identity matrix. In this paper, we model nematic tactoids using a three-dimensional \mathcal{Q} . By construction, \mathcal{Q} is symmetric and traceless, and both properties can be enforced by parameterization. In the isotropic phase, where there is no orientational order, $\mathcal{Q} = 0$, i.e., a zero-tensor. Given an instance of \mathcal{Q} , both \mathbf{n} and S can be reconstructed by eigenanalysis: the largest eigenvalue of \mathcal{Q} is $\frac{2}{3}S$ and \mathbf{n} is the associated normalized eigenvector. The \mathcal{Q} -tensor approach has a number of advantages over the director formulation. For one, it permits defects since when large gradients of \mathbf{n} arise, S compensates by tending to zero; it can accommodate defects with a non-integer winding number naturally. Moreover, it obviates the need to impose any unit-length constraints. Generally, these advantages are at the expense of requiring more degrees of freedom overall.

The local values of \mathcal{Q} are obtained by minimizing a free energy that includes bulk terms defined on a manifold, \mathcal{M} , and surface terms defined on the boundary $\partial\mathcal{M}$. The free energy has the form,

$$\mathcal{F}(\mathbf{x}, \mathcal{Q}, \nabla\mathcal{Q}, \dots) = \int_{\mathcal{M}} f(\mathbf{x}, \mathcal{Q}, \nabla\mathcal{Q}, \dots) d\mathbf{x} + \int_{\partial\mathcal{M}} g(\mathbf{x}, \mathcal{Q}, \nabla\mathcal{Q}, \dots) dS, \quad (2)$$

where $\mathbf{x} = (x_1, x_2, x_3) \in \mathcal{M}$ and f and g are linear or nonlinear energy densities that depend on \mathcal{Q} and its derivatives. The function g is defined on $\partial\mathcal{M}$ and may impose a preferred orientation of the LC relative to the boundary tangent plane, a phenomenon referred to as *anchoring*. Furthermore, the minimization may be subject to nonlinear *global* (integral) equality constraints, such as one that fixes the manifold's volume,

$$\mathcal{C}(\mathcal{Q}, \nabla\mathcal{Q}) = \int_{\mathcal{M}} c(\mathcal{Q}, \nabla\mathcal{Q}) d\mathbf{x} = 0. \quad (3)$$

2.1. Landau-De Gennes Energy Model

Absent any external forces, we specifically consider the one constant Landau-De Gennes model, where the free energy sufficient to capture the physics of nematic tactoids, \mathcal{F} , depends on the state variables of the system: the shape \mathcal{M} and the tensor $\mathcal{Q}(\mathbf{x})$. The free energy is,

$$\begin{aligned} \mathcal{F}(\mathbf{x}, \mathcal{Q}) = & \int_{\mathcal{M}} a \operatorname{tr}(\mathcal{Q}^2) + \frac{2b}{3} \operatorname{tr}(\mathcal{Q}^3) + \frac{c}{2} \operatorname{tr}(\mathcal{Q}^2)^2 + \frac{L_1}{2} |\nabla\mathcal{Q}|^2 d\mathbf{x} \\ & + \int_{\partial\mathcal{M}} \sigma - \frac{W}{2} \operatorname{tr}((\mathcal{Q} - \mathcal{Q}_s)^2) dS, \end{aligned} \quad (4)$$

where the first three bulk terms represent a Landau expansion of the free energy of \mathcal{Q} with Landau coefficients a , b , and c . These parameters, in effect, select a particular uniform value of S in the bulk; by convention, a is chosen to be temperature dependent, $a = a_0(T - T_0)$, where T_0 is the temperature below which the isotropic phase is no longer stable. The fourth term involving $\nabla\mathcal{Q}$ represents elasticity, and here, we adopt the commonly used one-constant approximation with a single elastic constant L_1 . On the boundary, $\partial\mathcal{M}$, the constant term with prefactor σ represents the isotropic surface tension. The second term is the anisotropic surface tension with anchoring coefficient W and is constructed to favor the alignment of the LC in the tangent plane of the boundary surface. Here, \mathcal{Q}_s is a Q -tensor with alignment in the normal direction of the surface,

$$\mathcal{Q}_s = S_0 \left(\boldsymbol{\nu} \otimes \boldsymbol{\nu} - \frac{\mathcal{I}}{d} \right), \quad (5)$$

where $\boldsymbol{\nu}$ is the local normal vector at the surface, S_0 is the degree of order induced by the surface, which may differ from the value set by the Landau coefficients in the bulk depending on the chemistry of the liquid crystal-host interface. The prefactor $W > 0$ controls the orientation such that, combined with the negative sign in front, higher values penalize the director's orientation toward the tangent plane. As discussed above, we impose a volume constraint,

$$\mathcal{C}(\mathbf{x}) = \int_{\mathcal{M}} d\mathbf{x} - V_0 = 0, \quad (6)$$

where, V_0 is the target volume of the tactoid.

In three dimensions, \mathcal{Q} can be parameterized to be symmetric and traceless,

$$\mathcal{Q} = \begin{bmatrix} q_{xx} & q_{xy} & q_{xz} \\ q_{xy} & q_{yy} & q_{yz} \\ q_{xz} & q_{yz} & -q_{xx} - q_{yy} \end{bmatrix}, \quad (7)$$

and hence includes five independent degrees of freedom $\{q_{xx}, q_{xy}, q_{xz}, q_{yy}, q_{yz}\}$. We nondimensionalize \mathcal{F} and \mathcal{C} by introducing a length scale ξ , so that

$\mathbf{x} \rightarrow \xi \bar{\mathbf{x}}$ where $\bar{\mathbf{x}}$ is non-dimensional, and divide (4) by L_1 to get,

$$\begin{aligned} \bar{\mathcal{F}}(\bar{\mathbf{x}}, \mathcal{Q}) &= \int_{\mathcal{M}} \bar{a} \operatorname{tr}(\mathcal{Q}^2) + \frac{2\bar{b}}{3} \operatorname{tr}(\mathcal{Q}^3) + \frac{\bar{c}}{2} \operatorname{tr}(\mathcal{Q}^2)^2 + \frac{1}{2} |\nabla \mathcal{Q}|^2 d\bar{\mathbf{x}} \\ &+ \int_{\partial \mathcal{M}} \bar{\tau} - \frac{\bar{\tau}\bar{\omega}}{2} \operatorname{tr}((\mathcal{Q} - \mathcal{Q}_s)^2) d\bar{S}, \end{aligned} \quad (8)$$

with dimensionless parameters,

$$\bar{a} = \frac{a\xi^3}{L_1}, \quad \bar{b} = \frac{b\xi^3}{L_1}, \quad \bar{c} = \frac{c\xi^3}{L_1}, \quad \bar{\tau} = \frac{\sigma\xi}{L_1}, \quad \bar{\omega} = \frac{W}{\sigma}. \quad (9)$$

The volume constraint, (6), is trivially non-dimensionalized, and hence we simply choose V_0 to be dimensionless. Note that \mathcal{Q} and S are also non-dimensional.

Hence, to find the equilibrium order and mesh configuration, we minimize (8) subject to the global nonlinear constraint, (6). For the rest of the paper, we assume all quantities are suitably nondimensionalized and drop the bar notation.

2.2. Discrete Energy Model

To set up the discrete optimization problem, we represent \mathcal{M} as a simplicial complex denoted by M consisting of p spatial coordinate points, $\mathbf{x}_i \in M$, $1 \leq i \leq p$ and N triangular or tetrahedral elements. Using linear finite elements, we discretize the Q-tensor, (7), over M with degrees of freedom defined as $Q_i := \mathcal{Q}(\mathbf{x}_i)$ at each point $\mathbf{x}_i \in M$. Note that this discretization leads to three DOFs for the each coordinate of \mathbf{x}_i , and five DOFs for the Q_i , one for each $\{q_{xx}, q_{xy}, q_{xz}, q_{yy}, q_{yz}\}$. Other finite-element approaches for Q-tensor models have been considered in [38, 41, 42], as well as for other LC frameworks [43, 44, 45].

Next, $\mathcal{F}(\mathbf{x}, \mathcal{Q})$ and $\mathcal{C}(\mathbf{x})$ are defined over M to obtain $F(\mathbf{x}, Q)$ and $C(\mathbf{x})$,

$$\begin{aligned} F(\mathbf{x}, Q) &= \int_M a \operatorname{tr}(Q^2) + \frac{2b}{3} \operatorname{tr}(Q^3) + \frac{c}{2} \operatorname{tr}(Q^2)^2 + \frac{1}{2} |\nabla Q|^2 d\mathbf{x} \\ &+ \int_{\partial M} \tau - \frac{\tau\omega}{2} \operatorname{tr}((Q - Q_s)^2) dS, \end{aligned} \quad (10)$$

$$C(\mathbf{x}) = \sum_{i=1}^N \operatorname{Vol}(T_i) - V_0, \quad (11)$$

where $\mathbf{x} \in M$ and Q is the set of degrees of freedom of the Q-tensor defined on M , and $\text{Vol}(T_i)$ is the volume of the i^{th} tetrahedra, T , in the simplicial complex. The corresponding discrete shape optimization problem is then defined as,

$$\begin{aligned} (M^*, Q^*) &= \arg \min_{\mathbf{x} \in M, Q} F(\mathbf{x}, Q), \\ \text{s.t. } & 0 = C(\mathbf{x}). \end{aligned} \tag{12}$$

Here, M^* and Q^* represent the equilibrium configurations of the manifold and the Q-tensor values at each point in M for the minimized configuration.

3. Energy Minimization of the Discrete Tactoid Energy

Considering the discrete (\mathbf{x}, Q) shape optimization problem, (12), we now describe both a GD-based and a Newton-based method. We note that the GD-based approach in [23] was formulated for a director formulation with a Frank-Oseen energy [39]; we, therefore, describe in the first subsection how the method is modified for the Q-tensor formulation used in this paper. Next, we discuss the quasi-Newton approach, which is the main target of this work, and nested iteration, which is used to improve the performance of both methods.

3.1. Gradient Descent

In [23], the authors note that the combined (\mathbf{x}, \mathbf{n}) optimization problem exhibited stiffness due to intrinsic differences in length scale between the vertex, \mathbf{x} , and director, \mathbf{n} , degrees of freedom. To alleviate this, they use an alternating gradient descent scheme, first taking descent steps in \mathbf{n} followed by \mathbf{x} and repeating until convergence. Given the connection between \mathbf{n} and Q , we use a similar approach.

Consider a vector of the spatial vertices at the k^{th} iteration, $\mathbf{x}^k \in M^k$, where M^k is the current triangulation of the grid, M . We first compute the gradients of F and C with respect to \mathbf{x} on the given grid M , denoted by F_M^k , and C_M^k , respectively, and evaluate each gradient at $\mathbf{x}_i \in M^k$. This trio of data, $\{\mathbf{x}^k, F_M^k, C_M^k\}$ is then projected onto the constraint's tangent space,

$$\tilde{\mathbf{x}}^k \leftarrow \mathbf{x}^k + \alpha_k \left(F_M^k - \frac{F_M^k \cdot C_M^k}{C_M^k \cdot C_M^k} C_M^k \right). \tag{13}$$

Here, α_k is the k^{th} -iteration step-size found from performing a one-dimensional line search. The update defined in (13) is an intermediate step towards finding $\mathbf{x}^{k+1} \in M^{k+1}$ since $\tilde{\mathbf{x}}^k$ only satisfies the constraint to linear order. Following [23], we perform additional reprojection steps,

$$\tilde{\mathbf{x}}^k \leftarrow \tilde{\mathbf{x}}^k + \frac{C(\tilde{\mathbf{x}}^k)}{C_M^k \cdot C_M^k} C_M^k. \quad (14)$$

In each reprojection step, C_M^k is evaluated at $\tilde{\mathbf{x}}_i \in \tilde{M}^k$. The prefactor, $\frac{C(\tilde{\mathbf{x}}^k)}{C_M^k \cdot C_M^k}$, represents the difference between the constraint value and its target; reprojection steps are repeated until the constraint is satisfied to a given tolerance. This projected value is used as the next iterate $\mathbf{x}^{k+1} \leftarrow \tilde{\mathbf{x}}^k$.

To find Q we follow a similar procedure but with $\{Q^k, F_Q^k\}$,

$$Q^{k+1} \leftarrow Q^k + \beta_k F_Q^k, \quad (15)$$

where β_k is obtained with a separate one-dimensional line search. A second projection is unnecessary as the global constraint only depends on $\mathbf{x} \in M$. In practice, [23] starts by optimizing for the field and then for the spatial coordinates. To control mesh quality, a procedure called *equiangularization* is used after a few iterations of each optimization routine. This ensures that no irregular triangles (i.e., long and skinny) appear in the discrete manifold, and is crucial when the amount of spatial or order deformation increases.

3.2. Quasi-Newton

The GD algorithm introduced in the previous section converges quite slowly and can stagnate under certain conditions. It also incorporates a number of metaparameters, such as the mesh quality control and the number of alternating iterations to be taken for shape and field degrees of freedom that must be hand-tuned for each problem. To address these issues, we develop a quasi-Newton (QN) based method to solve the full (\mathbf{x}, Q) minimization problem all at once. Given the presence of the nonlinear constraint, we introduce the Lagrangian \mathcal{L} of the system based on (12),

$$\mathcal{L}(\mathbf{x}, Q, \lambda) = F(\mathbf{x}, Q) - \lambda C(\mathbf{x}), \quad (16)$$

where $\lambda \in \mathbb{R}$. The necessary first-order optimality conditions for minimizing the Lagrangian are

$$\mathcal{L}_M := F_M - \lambda C_M = \mathbf{0}, \quad (17)$$

$$\mathcal{L}_Q := F_Q = \mathbf{0}, \quad (18)$$

$$\mathcal{L}_\lambda := -C(\mathbf{x}) = 0, \quad (19)$$

where F_M and F_Q are the first-order Gateaux derivatives with respect to every $\mathbf{x}_i \in M$ and Q_i on M , respectively (i.e., the gradients as computed for GD), and C_M is the gradient of the constraint with respect to each \mathbf{x}_i .

These equations are nonlinear, so we linearize (17)-(19) and set up the corresponding iterative scheme. Let $(\mathbf{x}^k, Q^k, \lambda^k)$ be the current approximations for (\mathbf{x}, Q, λ) , respectively. The update, $(\mathbf{d}_M, \mathbf{d}_Q, d_\lambda)$, to the approximation is the solution to the QN iteration,

$$\begin{bmatrix} \mathbf{d}_{M,Q} \\ d_\lambda \end{bmatrix} = \begin{bmatrix} \mathbf{B}^k & -(\mathbf{A}^k)^T \\ -\mathbf{A}^k & 0 \end{bmatrix}^{-1} \begin{bmatrix} \mathbf{R}^k \\ -\mathcal{L}_\lambda \end{bmatrix} =: \mathcal{A}^{-1} \mathcal{R}, \quad (20)$$

with

$$\mathbf{d}_{M,Q} = \begin{bmatrix} \mathbf{d}_M \\ \mathbf{d}_Q \end{bmatrix}, \quad \mathbf{A}^k = \begin{bmatrix} C_M & \mathbf{0} \end{bmatrix}, \quad \mathbf{R}^k = \begin{bmatrix} -\mathcal{L}_M \\ -\mathcal{L}_Q \end{bmatrix}.$$

Here, \mathbf{B}^k is an approximation to the Hessian of the (\mathbf{x}, Q) portion of the Lagrangian, denoted by $\nabla^2 \mathcal{L}^k := \begin{bmatrix} \mathcal{L}_{MM}^k & \mathcal{L}_{MQ}^k \\ \mathcal{L}_{QM}^k & \mathcal{L}_{QQ}^k \end{bmatrix}$, where the entries are second-order Gateaux derivatives with respect to the mesh and the Q -tensor at (\mathbf{x}^k, Q^k) . Additionally, \mathbf{A}^k contains the gradient of the constraint function at \mathbf{x}^k , and \mathbf{R}^k is the nonlinear residual for the (\mathbf{x}, Q) portion of the system. Since \mathcal{A} is a saddle-point matrix, which poses challenges for building efficient solvers, we choose a BFGS approximation and use explicit formulae to compute $\mathbf{H}^k = (\mathbf{B}^k)^{-1}$ and \mathcal{A}^{-1} [46]. This allows us to find a closed form for computing the updates $(\mathbf{d}_M, \mathbf{d}_Q, d_\lambda)$ which we use to set up a recursive matrix-free approach of implicitly updating the approximation of \mathbf{H}^k .

Next, we find the step size for the field, α_Q , and the step size for the spatial coordinates α_M . The step size α_Q is found with backtracking line search such that it satisfies,

$$F(\mathbf{x}^k, Q^k + \alpha_Q \mathbf{d}_Q) \leq F(\mathbf{x}^k, Q^k) + \eta \alpha_Q (F_Q^k)^T \mathbf{d}_Q, \quad (21)$$

where $\eta \in (0, 1)$. Then, we update the field accordingly,

$$Q^{k+1} \leftarrow Q^k + \alpha_Q \mathbf{d}_Q. \quad (22)$$

The step size α_M for the spatial coordinates is found using an ℓ^1 monitor function [47] defined as

$$\phi(\mathbf{x}, Q^k, \mu) := F(\mathbf{x}, Q^k) + \mu \|C(\mathbf{x})\|_1, \quad (23)$$

where $\mu \in \mathbb{R}$ is a penalty term for the constraint. This monitor function decides what factor of \mathbf{d}_M and d_λ should be accepted in order to decrease $F(\mathbf{x}^{k+1}, Q^k)$. Similar to finding α_Q , we use backtracking until the following inequality is satisfied,

$$\phi(\mathbf{x}^k + \alpha_M \mathbf{d}_M, Q^k, \mu_k) \leq \phi(M^k, Q^k, \mu_k) + \eta \alpha_M (\phi_M^k)^T \mathbf{d}_M,$$

where $\eta \in (0, 1)$, $\mu_k > \|\lambda_k\|_\infty + \rho$ (ρ is a positive constant), and

$$(\phi_M^k)^T \mathbf{d}_M := \alpha_M F_M^k \mathbf{d}_M - \mu_k \|C(\mathbf{x}^k)\|_1. \quad (24)$$

Finally, we update the spatial coordinates and Lagrange multiplier,

$$\mathbf{x}^{k+1} \leftarrow \mathbf{x}^k + \alpha_M \mathbf{d}_M \quad (25)$$

$$\lambda^{k+1} \leftarrow \lambda^k + \alpha_M d_\lambda. \quad (26)$$

Given that the constraint is prescribed only to the mesh, we allow for its respective Lagrange multiplier, λ^k , to have the same step size α_M as the mesh update.

Finally, we note that quasi-Newton methods have been extensively studied, and several convergence results have been established. For the BFGS approach we consider, a well-known result [25, Thm. 18.6] guarantees super-linear convergence of the method under certain assumptions. Though this result does not consider line search, for all of the tests presented here, the step sizes approach one as the method converges. The assumptions of the theorem include conditions on the continuity and differentiability of the objective and constraint function that can be shown by direct calculation. Moreover, there are conditions on the linear independence of the gradients of the constraints in order to guarantee that the first-order optimality conditions, (17)-(19), are satisfied. Since we only have one constraint here, this is trivially true. We also need to assume that the Hessian, $\nabla^2 \mathcal{L}$, at the local solution, (\mathbf{x}^*, Q^*)

and its initial approximation, \mathbf{B}^0 , are symmetric and positive definite. The latter is straightforward since $\mathbf{B}^0 = \delta\mathcal{I}$ with $\delta > 0$, while the former requires several assumptions on the physical parameters. The numerical experiments we present indicate that we are within the regime where this is satisfied. Finally, as with all Newton-based methods, we need the initial guess to be “good enough” in order for the iterates to remain in the basin of attraction. To guarantee this, we introduce the notion of nested iteration.

3.3. Nested Iteration

Both QN and GD, as described above, are sensitive to initial guesses. In particular, as the anisotropic surface tension parameters increase, we expect to see the nematic LC tactoids elongating towards the characteristic eye shape [14, 2]. Numerically, this means that by starting from the same initial guess for every parameter value, we may not be close to the basin of attraction for some regions of parameter space. This can lead the method to stagnate at locally optimal solutions, not the expected global minima. To remedy this issue, we wrap each method with nested iteration.

Nested iteration [27, 28] begins with an initial coarse grid, denoted by M_i with only a few vertex points, p , that represents the problem domain. This coarse grid may not capture all the details of the solution, but solving the nonlinear system on this grid is computationally inexpensive. Thus, (12) is solved on the coarse grid with either QN or GD until a preferred convergence criterion is reached. The coarse grid, M_i , is then subdivided into smaller elements. In this work, we consider uniform refinement such that each element is divided into four (for triangular elements) or eight (for tetrahedral elements) smaller elements. The coarse solution from M_i is then linearly interpolated onto the finer grid M_{i+1} and used as an initial guess for solving the problem now represented on M_{i+1} of size $8p$ (in three-dimensions) and $4p$ (in two-dimensions). This initial solution on M_{i+1} should then be a more accurate guess as it came from solving a similar problem on M_i , and thus fewer iterations to converge are expected.

Remark. *Through the use of nested iteration, we progressively improve the initial guess, (\mathbf{x}^0, Q^0) , thereby maintaining that $\|(\mathbf{x}^0, Q^0) - (\mathbf{x}^*, \mathbf{Q}^*)\|$ is sufficiently small. Consequently, this helps guarantee convergence results, such as those in [25].*

4. Numerical Results

We demonstrate the robustness of QN combined with Nested Iteration (NI) on challenging two-dimensional and three-dimensional problems involving the formation of a nematic tactoid. We compare the approach with the GD-based techniques described in Section 3.1. Numerical methods and benchmark tests are implemented and executed in *Morpho*, an open-source programmable environment for shape optimization [48]. *Morpho* is able to evaluate the objective function of interest as well as its gradients with respect to the configuration's and field's degrees of freedom. Furthermore, grid quality control in *Morpho* does not require user intervention and provides the user the option of automatic domain refinement and easy object-oriented programming. All timed numerical results are done using a workstation with an 8-core 3-GHz Intel Xeon Sandy Bridge CPU and 256 GB of RAM. Force and energy calculations in *Morpho* are parallelized using a symmetric multiprocessing model with a user-controllable number of worker threads. In the majority of the numerical experiments we report below, we use 16 worker threads; in a number of indicated cases we use fewer worker threads to conserve memory. For all timings reported, we do not include the time spent during refinement and equiangularization *between* nested iteration grids, because these components are not yet parallelized and are common to all methods.

Throughout this section, all test problems use material constants from [40] with $a_0 = 0.042 \times 10^6 \text{ Nm}^{-2} \text{ K}^{-1}$ and $T - T_0 = -0.1 \text{ K}$. Thus, the prefactors in the *dimensional* free energy, (4), are:

$$a = -0.042 \times 10^5 \text{ Nm}^{-2}, \quad b = -0.64 \times 10^6 \text{ Nm}^{-2}, \quad (27)$$

$$c = 0.35 \times 10^6 \text{ Nm}^{-2}, \quad L_1 = 1 \times 10^{-11} \text{ N}. \quad (28)$$

4.1. Two-Dimensional Nematic Tactoids

We begin by modeling two-dimensional nematic tactoids, where the computational domain represents a slice of an object that is infinitely extended in the perpendicular direction. We will investigate solutions where the nematic director lies in-plane on the computational domain, and hence \mathcal{Q} can be described by a reduced parameterization,

$$\mathcal{Q} = \begin{bmatrix} q_{xx} & q_{xy} & 0 \\ q_{xy} & \frac{1}{3} - q_{xx} & 0 \\ 0 & 0 & -\frac{1}{3} \end{bmatrix}, \quad (29)$$

that includes only two independent degrees of freedom q_{xx} and q_{xy} . We construct the preferred surface value of the Q tensor \mathcal{Q}_s in (8) from the local tangent vector \mathbf{t} on the boundary,

$$\mathcal{Q}_s = S_0 \left(\mathbf{t} \otimes \mathbf{t} - \frac{\mathcal{I}}{3} \right). \quad (30)$$

To favor alignment with the local tangent vector, we must prefactor the anchoring term in (10) with a positive sign,

$$\int_{\partial M} \tau + \frac{\tau\omega}{2} \text{tr}((Q - Q_s)^2) dS.$$

The volume constraint becomes a cross-sectional area constraint for a target area A_0 ,

$$\mathcal{C}(\mathbf{x}) = \int_{\mathcal{M}} d\mathbf{x} - A_0 = 0.$$

Consequently, the constraint has the discrete form,

$$\mathcal{C}(\mathbf{x}) = \sum_{i=1}^{p-2} \frac{1}{2} \|(\mathbf{x}_{i+1} - \mathbf{x}_i) \times (\mathbf{x}_{i+2} - \mathbf{x}_{i+1})\| - A_0.$$

It is convenient to use slightly different parameters from those listed in (9) for the two-dimensional geometry, because the energy functional (8) now has dimensions of energy per unit length; hence, it is convenient to pull out a common factor of ξ from the definitions (9). Setting $\xi = 1 \times 10^{-7} m$, then, the constants corresponding to those in the *non-dimensionalized* free energy, (10), are

$$\bar{a} = -4.2, \quad \bar{b} = -640, \quad \bar{c} = 350. \quad (31)$$

For the numerical experiments below, we let the surface tension, $\bar{\tau}$, vary from 1 to 100 and the surface anchoring, $\bar{\omega}$ vary from 0.01 to 1. This corresponds to a dimensionalized surface tension, σ , ranging from $10^{-4} - 10^{-2} N$ and anchoring values, W , ranging from $10^{-6} - 10^{-2} N$. Moreover, we artificially scale the Landau coefficients so that the defect size is ~ 10 its true value. The scalar order parameter S_0 for the tangential anchoring is initialized as,

$$S_0 = \frac{-\bar{b} + \sqrt{\bar{b}^2 - 24\bar{a}\bar{c}}}{4\bar{c}} = 0.933567.$$

For the rest of the section, we will refer to nondimensionalized quantities only and drop the bar notation.

For all test problems, the initial guess on the coarsest grid is defined on a circle of area 1 with equally distributed vertices representing the degrees of freedom, $\mathbf{x} \in M$. The initial director field is aligned parallel to the x -axis. We start by solving the discrete problem on the coarsest grid of size $|M_i| = 16$, where the notation $|M_i|$ denotes the number of vertices on grid M_i , and propagate the solution across nine levels of refinement until the finest grid of size $|M_i| = 591,361$. For both methods described in this work, after each level of refinement, we perform the equiangularization procedure mentioned above, that improves the quality of the mesh, ensuring there are no irregular elements. The preferred convergence criterion is the relative change in the energy F^k , with the tolerance set at 10^{-6} . We compare the results from the NI algorithm to those obtained running solely on the finest grid, M_9 . We compare the final energy, F^k , the runtime in seconds, and the number of iterations on each grid.

4.1.1. Fixed Shape and Fixed Field Subproblems

Before performing the full (\mathbf{x}, Q) optimization, we aim to understand the separate role of shape and Q degrees of freedom by defining two subproblems derived from (12):

Subproblem A (Fixed Shape)

$$Q^* = \arg \min_Q F(\mathbf{x}^*, Q); \quad (32)$$

Subproblem B (Fixed Field)

$$\begin{aligned} M^* &= \arg \min_{\mathbf{x} \in M} F(\mathbf{x}, Q^*), \\ \text{s.t. } & 0 = C(\mathbf{x}). \end{aligned} \quad (33)$$

These subproblems are used to motivate the use of our QN-based method. Therefore, we do not compare it with the gradient descent method. In Subproblem A, (32), which we call the Fixed Shape model, we assume the grid, M^* , with vertices \mathbf{x}^* is fixed and at equilibrium. Similarly, for Subproblem B, (33), which we call the Fixed Field model, the field, or Q-tensor, Q^* defined on M , is fixed and at equilibrium.

Solutions to the Fixed Shape model are director fields with different alignments strongly affected by the isotropic surface tension τ while the anchoring parameter remains small at $\omega = 0.2$. The boundary terms from (32) can be split into two parts: the line tension integral,

$$\tau \int_{\partial M} dl, \quad (34)$$

and the surface anchoring integral,

$$\frac{\tau\omega}{2} \int_{\partial M} \text{tr}(Q - Q_s)^2 dl. \quad (35)$$

With the grid fixed, as we increase τ , we only see an effect from the surface anchoring integral, (35), as it depends on the Q-tensor. Here, the prefactor $\Gamma := \frac{\tau\omega}{2}$ promotes stronger tangential anchoring as τ increases. Following Bates' conclusion [13], we expect to see stronger tangential alignment on the domain's boundary as τ increases as well as the emergence of two defects [4, 5] that become physicalized in the domain. This is confirmed in Figures 1 and 2.

We compare the results of QN with and without nested iteration for various values of τ on grids up to M_9 . We retain the overall shape of the domain, a dodecagon, from the coarsest grid. The left graphics of Figures 1 and 2 show the distribution of the scalar order parameter S , and the corresponding director field is given on the right. Both standalone QN and QN with NI depict two defects appearing with stronger surface anchoring, as expected. Both methods also demonstrate that the director field anchors tangentially to the boundary as τ tends to 100. We note that while the solutions from nested iteration locate the defect pair near two opposing vertices of the polygonal boundary, we also see a rotational invariance in the energy. Nevertheless, the two methods have converged to similar energies.

Table 1 depicts the number of QN iterations both on grid M_9 alone (in parenthesis) and using NI to build to M_9 , showing the iteration count on each level of refinement. For small values of τ , the initial guess improves along the grids in the nested iteration process, thereby requiring fewer iterations to find the equilibrium solution on the finer grids. For increasing values of τ , while each level's iterations increase, we still see it decreasing down the levels, as expected. The table also shows the converged energy, F^k , and the runtime in seconds for the simulations. We see that both QN alone and

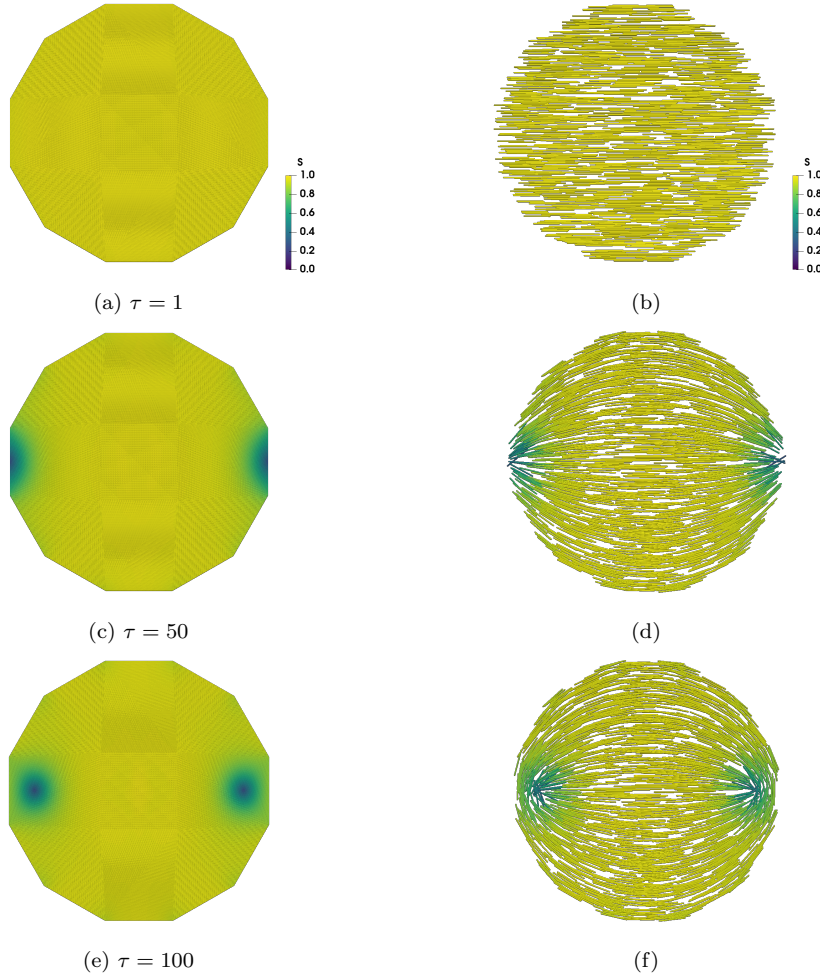


Figure 1: Applying QN for Subproblem A (Fixed Shape). Results shown on grid M_9 . The color bar indicates the value of S , i.e., the order of the director field in the domain. Left plots, (a), (c), (e), depict the order's distribution, illustrating two defects for higher τ . Right plots, (b), (d), (f), show the directors' anchoring to the boundary as $\tau \rightarrow 100$ and also demonstrate the disorder around the defects.

with NI yield the very similar converged solutions that minimize the energy. However, the addition of nested iteration allows the method to converge to a slightly lower energy which is physically expected. NI significantly improves the timing compared to standalone QN by a factor of 24 to 245 times.

Conversely, solutions to the Fixed Field model, (33), are the various shapes that result at a fixed $\tau = 10$, but varying ω . With the molecular

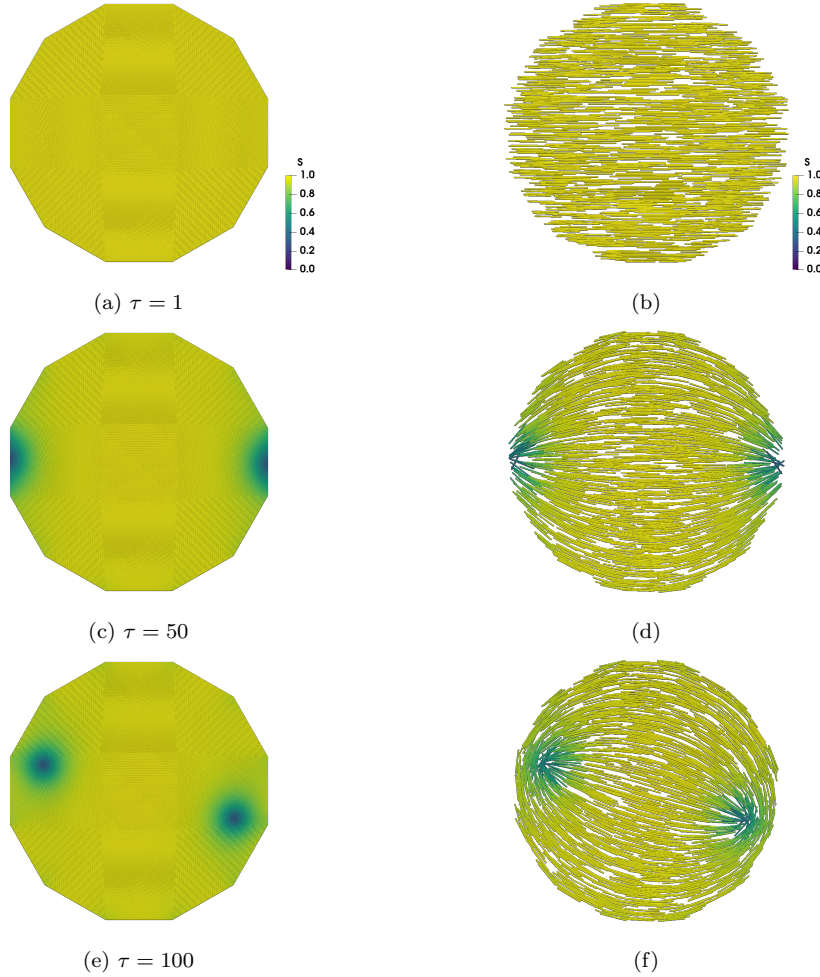


Figure 2: Applying QN with NI for Subproblem A (Fixed Shape). Results shown on grid M_9 . The color bar indicates the value of S , i.e., the order of the director field in the domain. Left plots, (a), (c), (e), depict the order's distribution illustrating two defects for higher τ . Right plots, (b), (d), (f), show the directors' anchoring to the boundary as $\tau \rightarrow 100$ and also demonstrate the disorder around the defects.

alignment fixed across the shape, we see an effect from both line tension (34) and anchoring (35) integrals, as Γ now indicates stronger *anisotropic* surface tension on the spatial coordinates of the nematic LC molecules. The increasing elongation of the shape illustrates this. As Prinsen and van der Schoot show [2], the tactoid morphology depends on the balance of surface and bulk forces and on the ratio of the anisotropic to isotropic surface ten-

		$\tau = 1$	5	10	50	100
NI Grid	$ M_i $	Iterations				
M_1	16	19	26	25	37	32
M_2	49	5	17	21	22	83
M_3	169	3	10	10	20	35
M_4	625	5	10	13	16	17
M_5	2,401	2	9	10	12	16
M_6	9,409	2	8	8	11	12
M_7	37,249	1	1	1	8	10
M_8	148,225	1	4	5	6	8
M_9	591,361	1 (35)	1 (79)	1 (549)	3 (666)	4 (851)
F^k		-19.87 (-19.85)	-18.73 (-18.65)	-17.53 (-17.53)	-12.99 (-12.98)	-12.04 (-12.01)
Runtime [sec]		37.32 (925.66)	67.79 (2,122.25)	75.53 (18,553.0)	154.34 (22,792.3)	200.84 (31,390.7)

Table 1: Subproblem A (Fixed Shape): Iteration count for QN with NI on each grid level. Iteration count for QN without NI is given on level M_9 in parenthesis. The grid size, $|M_i|$, final energy, F^k , and runtime in seconds, in bold, for the full simulation of QN with NI (standalone QN in parenthesis) are also given. NI improves efficiency in terms of iteration and runtime by taking minimal steps on the finest grid.

sion, $\frac{\Gamma}{\tau}$. With the molecular alignment fixed, their results illustrate that for $\omega \ll 1$, the aspect ratio is expected to scale as $1 + \omega$. Even though we fix $\tau = 10$ and bulk constants, a, b, c in the Fixed Field model, we mimic their results numerically by increasing ω from 0.01 to 1 indicating that the shape's aspect ratio is ω -dependent (see Figure 7).

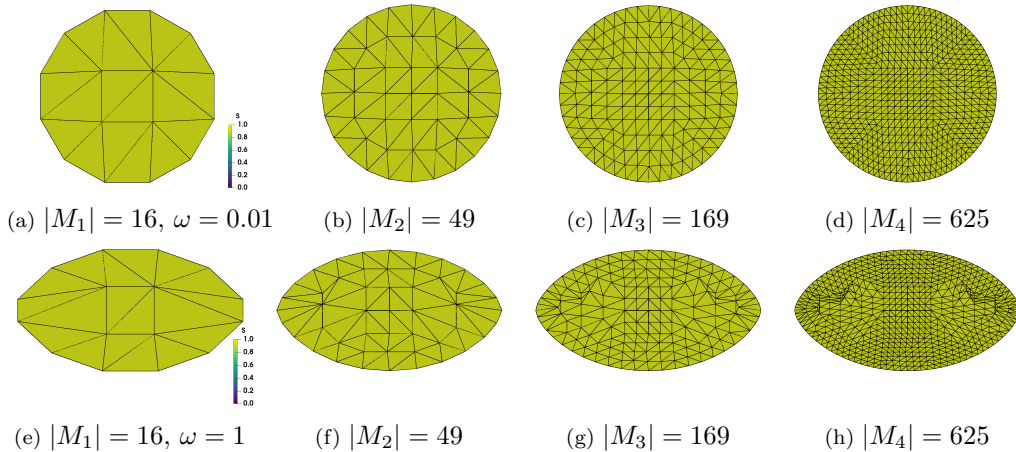


Figure 3: Applying QN with NI for Subproblem B (Fixed Field): Grids for each NI level for $\omega = 0.01$ (top row) and $\omega = 1$ (bottom row). Calculations on finer grids $M_5 - M_9$ are not shown because the structure is difficult to visualize.

We do not present standalone QN results as these did not converge for ev-

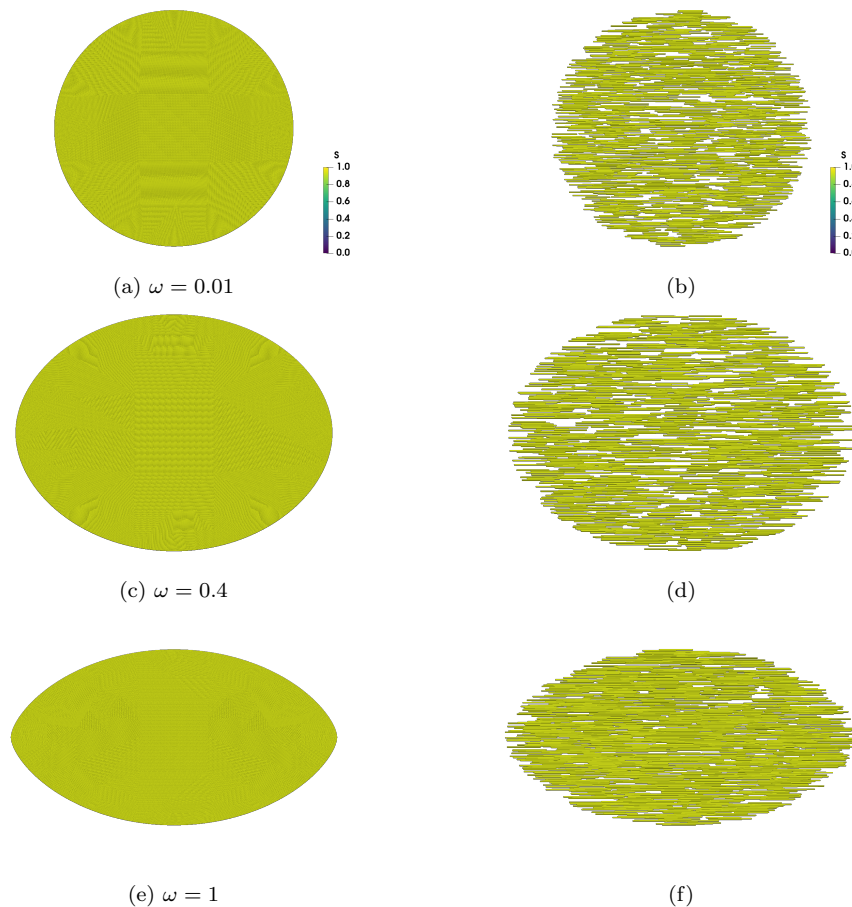


Figure 4: Applying QN with NI for Subproblem B (Fixed Field). Results shown on grid M_9 . The color bar indicates the value of S , i.e., the order of the director field in the domain. Left plots, (a), (c), (e), depict the order's distribution. Right plots, (b), (d), (f), show the fixed horizontally-aligned directors. Dramatic shape change is shown as $\omega \rightarrow 1$.

ery value of ω . As the shape changes, the initial circular guess is further from the optimal configuration, causing the method to stagnate. As expected, NI improves the initial guesses on each successive grid level, providing convergent results. Figure 3 displays the hierarchy of adaptive grids, before any mesh regularization, used in the simulation for the extreme ends of shape change (i.e., $\omega = 0.01$ and $\omega = 1$). Each refined grid, M_i is produced by quadrisecting the coarser elements from M_{i-1} . After each grid refinement, we regularize with equiangularization as a way to maintain a regular triangulation. In Figure

4, we again show the distribution of the scalar order parameter S (left plots), and the corresponding director field (right plots). We see the aspect ratio of the shape increasing as ω increases, validating Prinsen and van der Schoot’s theory. Note that with the Q held constant, the order of the director field is fixed at $S_0 = 0.933567$, and each director is horizontal to the x -axis. We do not expect to see defects virtualizing, only the tactoid elongating as the anisotropic surface tension strength increases.

4.1.2. Full (\mathbf{x}, Q) Optimization

The previous subproblems allow us to understand the individual effect on the presence of defects with τ and on the shape’s trend of deformation driven by ω . Numerically, we demonstrated that nested iteration significantly improved timings for examples with high orientational deformations and a notable improvement in convergence for regions of high spatial deformations. In this section, we allow both spatial and orientational movements, with the intention of comparing QN, derived in Section 3.2, with the GD method in Section 3.1, and seeing the effect of NI on both approaches.

We validate the same results from Subproblems A (32) and B (33), while tracking the distribution of the scalar order parameter S , the corresponding director field, the converged energy F^k , the number of iterations for each grid level, and the runtime in seconds. In these numerical experiments, we mimic the Fixed Field model (33) tests by holding τ fixed at 10 and varying ω from 0.01 to 1. Since we allow for spatial and orientational displacements at once, we expect to see an effect from both isotropic surface tension (34) and anchoring (35) effects. Visually, in this case, we see the colloidal particles elongating and virtualizing two defects on the opposite ends of the shape as ω tends to 1. This is the combined effect of the dynamic interplay of the isotropic and anisotropic strengths on tactoids.

Similarly to the previous subproblems, we show the NI grid progression on the levels for $\omega = 0.01$ and $\omega = 1$. Figure 5 illustrates the finite-element mesh evenly distributed throughout the grids in the absence of defects ($\omega = 0.01$). For $\omega = 1$, the vertices of the mesh collect around the two defects as the grids get finer, indicating that the defects are virtualizing as the shape is elongated and the directors are collecting around the defect’s region. For this problem, we also perform equiangularization after each grid refinement to maintain decent mesh quality.

Next, Figure 6 exhibits the combined effects from shape change and orientational variance as ω tends to 1 using QN with NI. The left graphics of

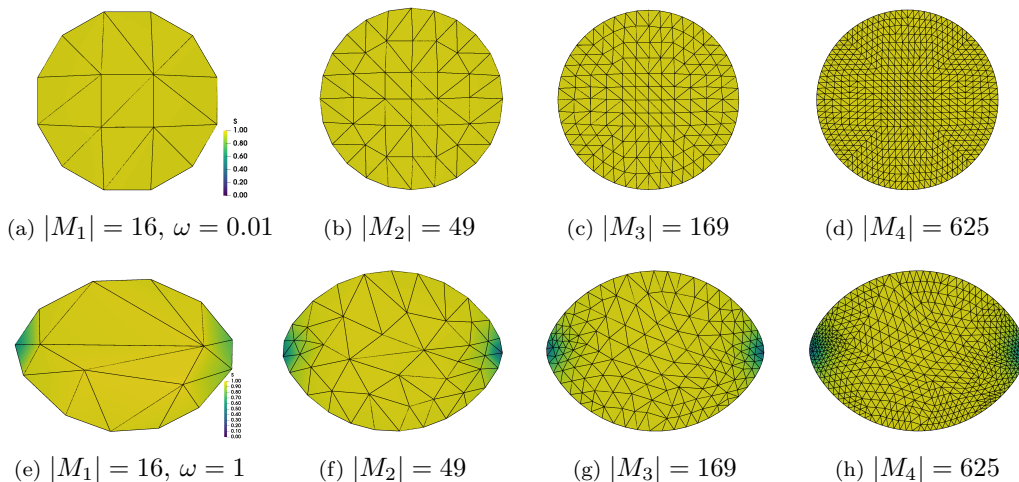


Figure 5: Applying QN with NI for full (\mathbf{x}, Q) 2D problem: Grids for each NI level for $\omega = 0.01$ (top row) and $\omega = 1$ (bottom row). Calculations on finer grids $M_5 - M_9$ are not shown because the structure is difficult to visualize.

the figure show the distribution of the scalar order parameter S , and the corresponding director field is given on the right. As expected, we see non-spherical shapes with increasing anisotropic surface tension. Consequently, we see the director field anchoring to the boundary as the prefactor Γ increases in the anchoring integral (35). Mimicking results in [13], defects appear as the shape elongates. As discussed for Subproblem A (Fixed Shape) (32), our procedure does find rotationally invariant solutions. Finally, corroborating results found in [2] and [48], Figure 7 shows the relationship between aspect ratio of the shape to anchoring strength, ω . We see a strong logarithmic trend in aspect ratio in the presence of changing molecular alignment (full problem) in contrast to a linear trend for fixed alignment (Subproblem B) as predicting by the scaling analysis done in [2].

To compare the performance of GD and QN with and without NI, iteration counts, final energy, and runtimes are included in Table 2. Runtime for standalone GD and GD with NI includes time for equiangularization within each grid as numerical experiments indicated it is crucial for convergence. Standalone QN and QN with NI, however, do not require equiangularization within each grid. NI yields significant improvement for both GD and QN. We note that sensitivity to spatial deformation depends on grid size, as QN and GD both met the preferred convergence criterion of a relative energy change on

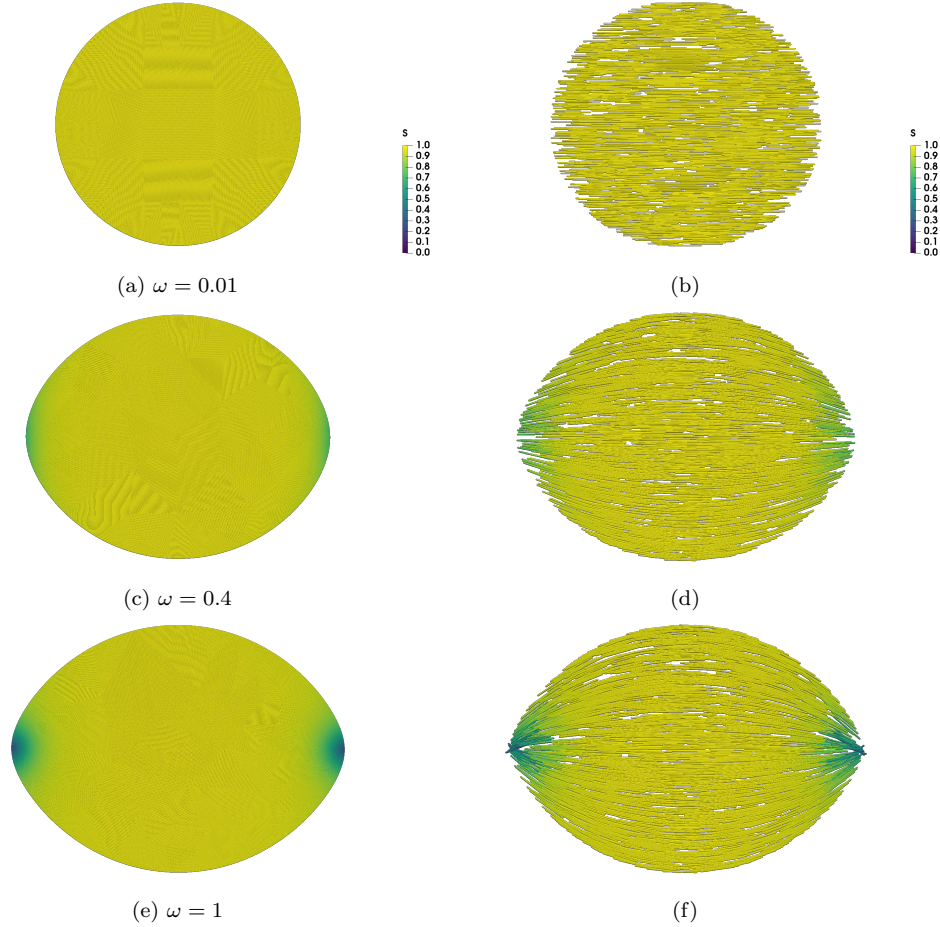


Figure 6: Applying QN with NI to full (\mathbf{x}, Q) 2D problem. Results shown on grid M_9 . The color bar indicates the value of S , i.e., the order of the director field in the domain. Left plots, (a), (c), (e), depict the order's distribution. Right plots, (b), (d), (f), show the directors with stronger anchoring as the shape changes with $\omega \rightarrow 1$. Areas in green indicate less order, showing the appearance of the defects, as expected.

the standalone M_9 grid simulations across all values ω , but converged to a different energy, approximately 0.1 – 1% higher than the energies computed with nested iteration. Thus, NI yields better variational estimates of the true continuum solution. With NI, the iteration counts for the full shape optimization problem dramatically decrease as we refine the grid to M_9 , guiding both methods to converge to the same final energy F^k (again lower than the energy found from the standalone methods). In addition, while GD with NI

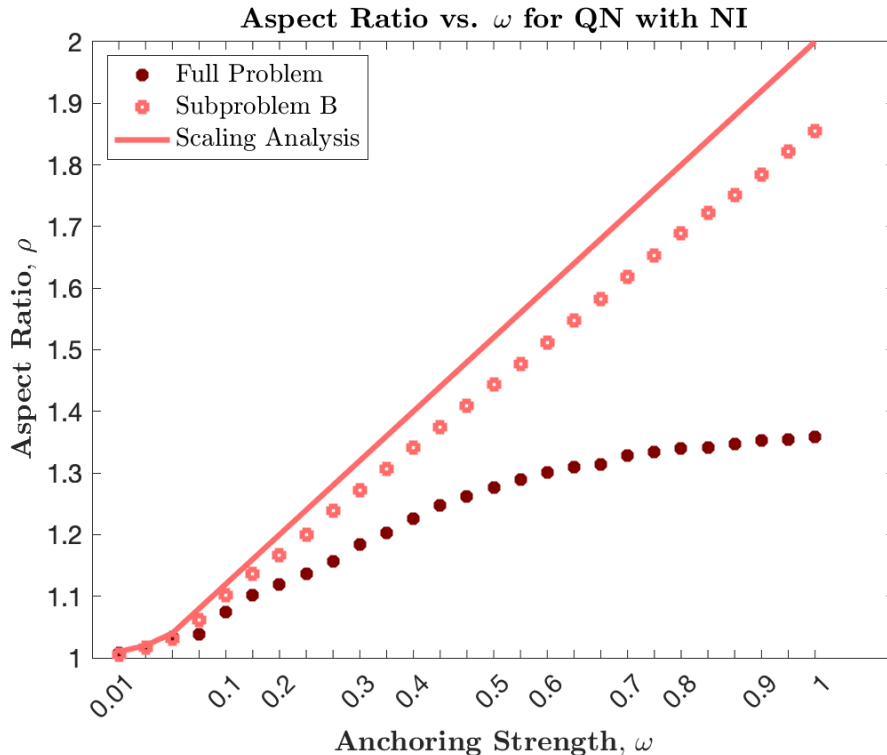


Figure 7: Applying QN with NI to full (\mathbf{x}, Q) 2D problem and Subproblem B: With the presence of molecular alignment (dark red) for the full problem, we see a logarithmic effect in aspect ratio compared to the linear trend (light red) for fixed alignment in Subproblem B. For fixed alignment, this is in agreement with the scaling analysis of [2] (solid line).

still requires several iterations for large ω on the finest grid, QN with NI converged in only a couple of iterations on the finest grid. As shown in Table 2, GD with NI significantly improves the timing compared to standalone GD by a factor of 53 to 219 times. Moreover, QN with NI improves the standalone QN timings by a factor of 3 to 52. The latter speedup factor is lower since standalone QN runs up to 28 times faster than standalone GD.

4.2. Three-Dimensional Nematic Tactoids

We conclude the numerical results section by simulating the spatial and orientational configuration of a challenging three-dimensional problem involving the formation of a nematic tactoid. We use the same material constants as above [40], with $\xi = 1 \times 10^{-7}m$ and, as before, we report the dis-

GD with NI		$\omega = 0.01$	0.2	0.4	0.6	0.8	1
NI Grid	$ M_i $	Iterations					
M_1	16	40	517	568	512	336	328
M_2	49	16	454	341	430	996	240
M_3	169	8	15	22	95	128	152
M_4	625	7	16	15	23	24	40
M_5	2,401	6	8	14	13	15	16
M_6	9,409	5	7	8	8	8	12
M_7	37,249	5	7	7	7	7	7
M_8	148,225	5	6	7	7	7	7
M_9	591,361	5 (1,151)	5 (535)	5 (478)	6 (2,036)	7 (1,956)	7 (2,070)
F^k		15.41 (15.83)	17.69 (18.78)	19.16 (21.70)	20.10 (24.13)	20.71 (26.63)	21.13 (29.01)
Runtime [sec]		213.59 (38,530.90)	239.56 (15,037.50)	241.70 (12,898.20)	250.78 (54,938.78)	259.96 (52,780.08)	260.56 (55,856.21)
QN with NI		$\omega = 0.01$	0.2	0.4	0.6	0.8	1
NI Grid	$ M_i $	Iterations					
M_1	16	16	178	161	176	115	111
M_2	49	10	25	97	55	163	112
M_3	169	4	17	24	68	18	60
M_4	625	4	10	9	12	26	12
M_5	2,401	3	7	8	10	9	8
M_6	9,409	2	7	6	5	6	7
M_7	372,49	2	4	7	6	3	4
M_8	148,225	2	2	2	5	3	2
M_9	591,361	2 (36)	2 (10)	2 (79)	2 (96)	2 (152)	2 (107)
F^k		15.41 (15.83)	17.69 (18.93)	19.16 (21.12)	20.10 (23.19)	20.71 (24.56)	21.12 (28.4271)
Runtime [sec]		132.89 (2,053.69)	166.13 (534.58)	165.99 (4,013.73)	201.77 (5,095.24)	169.76 (8,839.64)	159.02 (5,373.47)

Table 2: Full (\mathbf{x}, Q) 2D problem: Iteration count for GD with NI (top) and QN with NI (bottom) on each grid level. Iteration count for methods without NI is given on level M_9 in parenthesis. The final energy, F^k , and runtime in seconds for the full simulation with NI and without in parenthesis are also given.

tribution of the scalar order parameter, S , the corresponding director field, the converged energy, F^k , the number of iterations for each grid level of the QN-NI scheme, and the runtime in seconds. For the numerical experiments below, we fix the surface tension, $\tau = 10$, and vary the surface anchoring, ω from 0.01 to 0.18. The preferred convergence criterion is similarly the relative change in the energy F^k , this time with the tolerance set at 10^{-4} .

Recall that $|M_i|$ denotes the number of vertices on grid M_i . Here in three dimensions, we consider 6 different grids of increasing size, ranging from $|M_1| = 27$ to $|M_6| = 275,793$. Note that there are *eight* degrees of freedom attached to each grid point, and the actual number of vertices on each level might vary depending on the aspect ratio of the current configuration.

For the first value of ω ($\omega = 0.01$) we consider, the initial guess is defined on a sphere with volume 1 with equally distributed vertices representing the degrees of freedom, $\mathbf{x} \in M_1$. The initial director field, $\mathbf{n} = (1, 0, 0)$, is aligned parallel to the x -axis. However, as we see numerically, the shape's aspect ratio is linearly ω -dependent, much stronger than the logarithmic ω -dependence from the two-dimensional tactoid shapes seen earlier. Thus, the initial guess of a sphere is not adequate for convergence as ω is increased.

To mitigate this, we incorporate continuation with respect to ω on the coarsest grid, M_1 . From there, nested iteration is implemented as before. For example, the final equilibrium state on grid M_1 using $\omega = 0.01$ is used as the initial guess for the simulation of $\omega = 0.02$ on grid M_1 . The final state for $\omega = 0.02$ on grid M_1 is then used for the $\omega = 0.04$ simulation on the coarsest grid and so on.

Table 3 depicts the number of QN iterations using NI to build up through the hierarchy of grids, showing the iteration count on each level of refinement. For small ω , while the iterations eventually decrease to one iteration on the finest grid, we see that the coarsest grid of only 27 points is not enough to accurately represent the true shape and order, corroborated by the higher iteration count on grid M_2 . Therefore, for $\omega = 0.08$ to $\omega = 0.18$, shown in the bottom of Table 3, we start the nested iteration process using grid M_2 as the coarsest grid, and iterate to grid M_6 to keep 5 levels of refinement as before. Concurrently, we use continuation on ω across grid M_2 . Again, the results show the iteration count decreasing down the grids as ω increases, as expected. This iteration trend also implies that modeling these complex configurations requires more points to accurately represent the shape and order.

Figure 8 illustrates the nematic tactoids for increasing ω with the left column showing the order parameter, S , indicating the two defects on opposite sides. The right column depicts the strong tangential alignment of the directors to the boundary as ω increases. As ω increases, the regions of disorder have even less variance indicating that the two defects have localized at the opposite ends of the elongated tactoid. Similar to the two-dimensional simulations, stronger tangential anchoring brought on by higher $\frac{\tau\omega}{2}$ demonstrates significant orientation deformation and sizable spatial horizontal deformation. Furthermore, Figure 9 shows the aspect ratio of the shapes demonstrating a linear trend, unlike the logarithmic one seen in the two-dimensional tactoid shapes shown in Figure 7. Again, this sharper increase in aspect ratio between the initial spherical state and highly elongated final configurations motivated our use of continuation on ω along the coarsest grid.

Finally, we can push the bounds of admissible ω further to $\omega = 0.2$ and $\omega = 0.3$ by using continuation on all nested iteration levels, not just the coarsest. More specifically, for the first level M_1 , we use the converged solution on M_1 from the previous ω value as an initial guess, then for the second level, we refine that converged solution to M_2 , average it with the

		$\omega = 0.01$	0.02	0.04	0.06
NI Grid	$ M_i $	Iterations			
M_1	27	3	1	1	5
M_2	125	9	9	11	11
M_3	729	4	8	5	9
M_4	4,913	4	4	4	5
M_5	35,937	1	1	1	1
F^k		27.62	27.32	26.73	26.09
Runtime [sec]		475.76	492.62	491.32	545.69

		$\omega = 0.08$	0.10	0.12	0.14	0.16	0.18
NI Grid	$ M_i $	Iterations					
M_1	27						
M_2	125	13	15	15	14	20	18
M_3	729	8	11	7	6	6	7
M_4	4,913	5	5	5	6	6	7
M_5	36,025	3	3	3	3	5	5
M_6	275,793	1	1	1	1	1	3
F^k		25.42	24.73	24.02	23.28	22.50	21.69
Runtime [sec]		14,021.8	13,928.3	13,782.3	13,946.7	27,739.20*	35,083.5

Table 3: Full (\mathbf{x}, Q) 3D problem with $\omega = 0.01 \rightarrow 0.06$ (top) and $\omega = 0.08 \rightarrow 0.18$ (bottom): Iteration count for QN with NI on each grid level. The final energy, F^k , and runtime in seconds for the full simulation with NI are also given. *For $\omega = 0.16$, we use 8 worker threads instead of 16 to conserve memory.

converged solution on M_2 from the previous ω and use that as the initial guess for M_2 for the current ω . We continue this process until the desired level is reached. Figure 10 illustrates the tactoid shapes with the order measured by S on the left showing the two defects on the opposite ends of the shape, and the director field on the right strongly anchored tangentially to the shape’s boundary. We present this discussion as a precursor to our future work of combining continuation and nested iteration more rigorously.

5. Conclusion and Future Work

The present work describes an “all-in-one” quasi-Newton approach to modeling a challenging class of nematic liquid crystal tactoid shape optimization problems, where the equilibrium configuration of the model is found by minimizing a free energy functional with respect to the orientational order and shape of the domain. The approach is effective for this class of problems

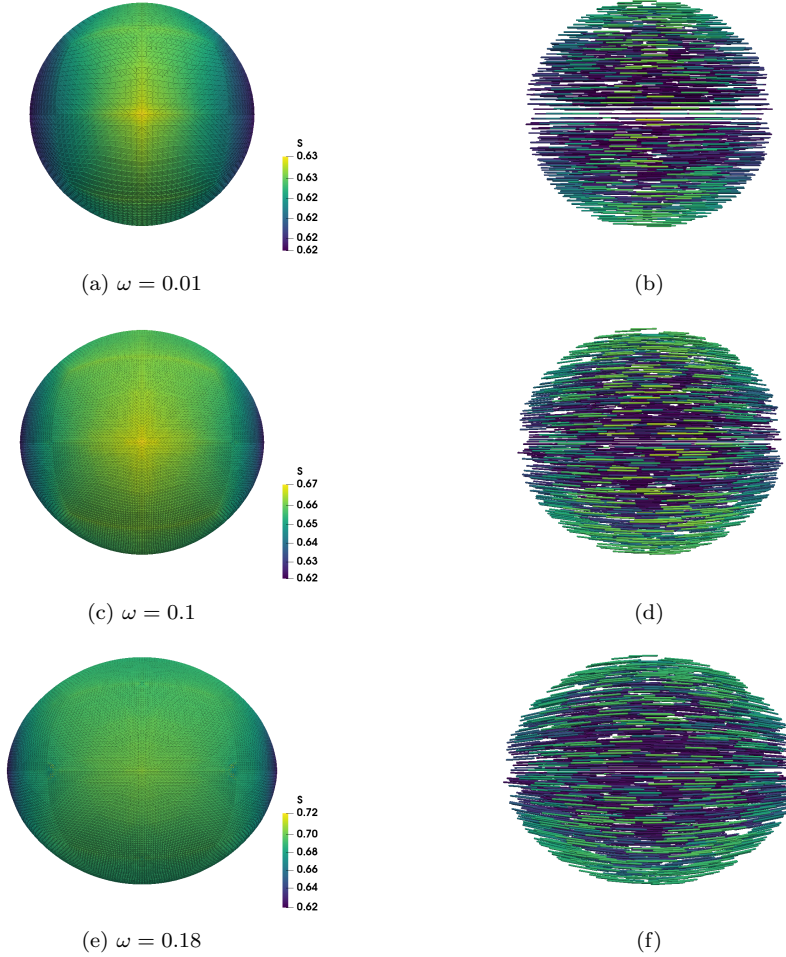


Figure 8: Applying QN with NI to full (\mathbf{x}, Q) 3D problem. The color bar indicates the value of S , i.e., the order of the director field in the domain. Left plots, (a), (c), (e), depict the order's distribution. Right plots, (b), (d), (f), show the directors with stronger anchoring as the shape changes with ω . Areas in dark green indicate less order, showing the appearance of the defects, as expected.

as it does not require maintenance of mesh quality during the minimization process, has an accurate line search procedure that dynamically updates all unknown variables simultaneously, and allows one to efficiently simulate the solutions on a large scale by uniformly increasing the resolution via nested iteration.

Exploring the space of shapes as a function of surface tension and anisotropic

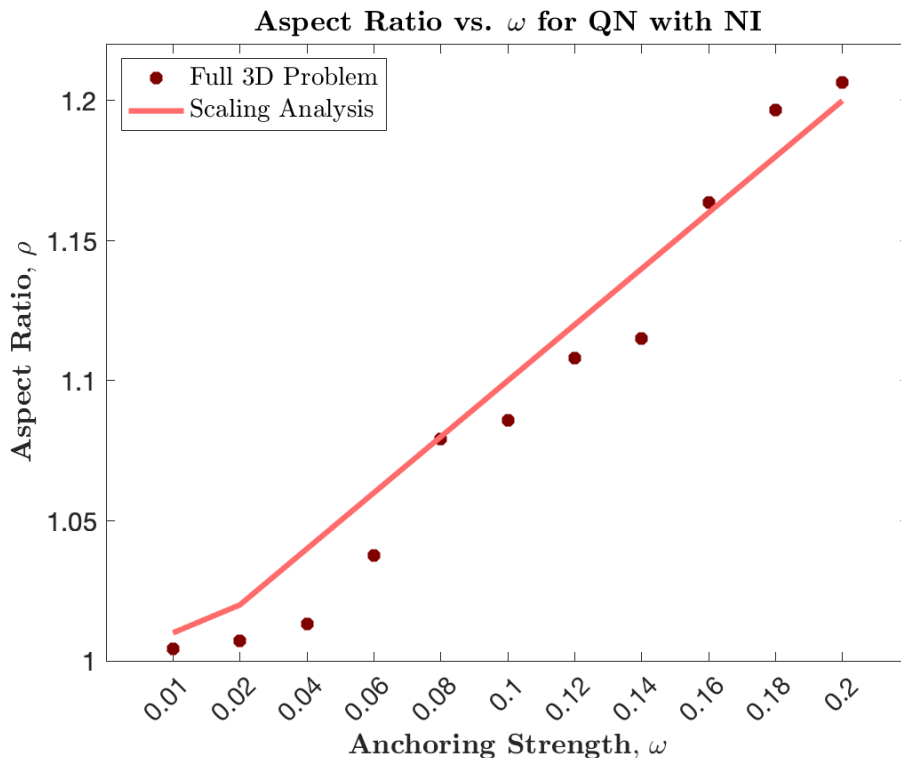


Figure 9: Applying QN with NI to full (\mathbf{x}, Q) 3D problem: With the presence of molecular alignment (dark red) for the full problem, we see a linear effect in aspect ratio (dark red) in agreement with the scaling analysis for 3D from [2] (solid line).

elastic constants, we find the nematic tactoids forming under conditions similar to those observed elsewhere [2, 13]. Our main goal here was to improve existing numerical algorithms used to find the equilibrium configurations while ensuring physical validity. We found that through the use of nested iteration, where we gradually refine the initial guess towards a solution with high resolution, we are able to preserve accuracy and robustness with low computational costs.

Future work involves solving the linearized steps iteratively using multi-grid methods to reduce the computational cost further while maintaining the same level of accuracy and efficiency. We also plan to further investigate the use of continuation coupled with nested iteration. In addition, we plan to apply the methods discussed in this work to other liquid crystal phases, e.g. cholesterics and smectics, and compare them against experimental re-

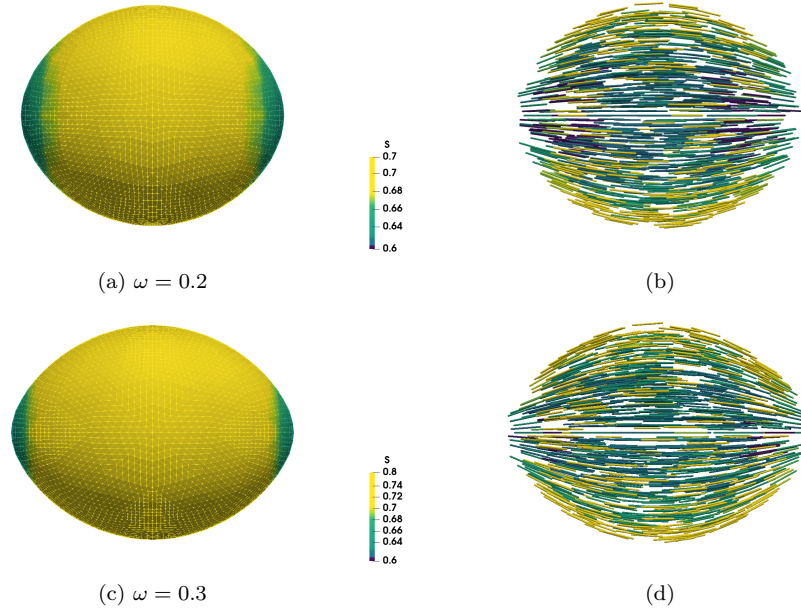


Figure 10: Applying QN with NI to full (\mathbf{x}, Q) 3D problem for $\omega = 0.2$ and $\omega = 0.3$. The color bar indicates the value of S , i.e., the order of the director field in the domain. Left plots, (a), (c), depict the order's distribution. Right plots, (b), (d), show the directors with stronger anchoring as the shape changes. Areas in green indicate less order, showing the appearance of the defects, as expected.

sults. Finally, including the study of inequality constraints that simulate the formation of nematic tactoids in bounded channels will be considered.

Acknowledgments

This work was supported by the National Science Foundation under Grant No. ACI-2003820. The authors of this paper would like to thank Dr. Xiaozhe Hu, Dr. Chaitanya Joshi, and Dr. Viviana Betancur for their valuable discussions.

References

- [1] P.-G. D. Gennes, J. Prost, The physics of liquid crystals, Oxford university press, 1993.

- [2] P. Prinsen, P. V. D. Schoot, Shape and director-field transformation of tactoids, *Physical Review E* 68 (2003) 1–11. doi:<https://doi.org/10.1103/PhysRevE.68.021701>.
- [3] S. Chandrasekhar, Surface tension of liquid crystals, *Molecular Crystals and Liquid Crystals* 2 (1966) 71–80. doi:<https://doi.org/10.1080/15421406608083061>.
- [4] J. Dzubiella, M. Schmidt, H. Löwen, Topological defects in nematic droplets of hard spherocylinders, *Physical Review E* 62 (2000) 5081–5091.
- [5] C. E. Sitta, F. Smallenburg, R. Wittkowski, H. Löwen, Liquid crystals of hard rectangles on flat and cylindrical manifolds, *Physical Chemistry Chemical Physics* 20 (2018) 5285–5294. doi:<https://doi.org/10.1039/C7CP07026H>.
- [6] J. P. F. Lagerwall, G. Scalia, A new era for liquid crystal research: Applications of liquid crystals in soft matter nano-, bio-and microtechnology, *Current Applied Physics* 12 (2012) 1387–1412. doi:<https://doi.org/10.1016/j.cap.2012.03.019>.
- [7] P. der Asdonk, P. H. J. Kouwer, Liquid crystal templating as an approach to spatially and temporally organise soft matter, *Chemical Society Reviews* 46 (2017) 5935–5949. doi:<https://doi.org/10.1039/C7CS00029D>.
- [8] S. T. Stealey, A. K. Gaharwar, S. P. Zustiak, Laponite-based nanocomposite hydrogels for drug delivery applications, *Pharmaceuticals* 16 (2023) 1–19. doi:[10.3390/ph16060821](https://doi.org/10.3390/ph16060821).
- [9] R. Mascarenhas, G. Kaur, Electrically conductive polymer-clay nanocomposites, Vol. 2535, 2023, pp. 1–15. doi:<https://doi.org/10.1063/5.0115418>.
- [10] M. Wehner, R. L. Truby, D. J. Fitzgerald, B. Mosadegh, G. M. Whitesides, J. A. Lewis, R. J. Wood, An integrated design and fabrication strategy for entirely soft, autonomous robots, *nature* 536 (2016) 451–455. doi:[10.1038/nature19100](https://doi.org/10.1038/nature19100).

- [11] D. S. Shah, J. P. Powers, L. G. Tilton, S. Kriegman, J. Bongard, R. Kramer-Bottiglio, A soft robot that adapts to environments through shape change, *Nature Machine Intelligence* 3 (2021) 51–59. doi:<https://doi.org/10.1038/s42256-020-00263-1>.
- [12] F. J. Schwarzendahl, P. Ronceray, K. L. Weirich, K. Dasbiswas, Self-organization and shape change by active polarization in nematic droplets, *Physical Review Research* 3 (2021) 1–6. doi:<https://doi.org/10.1103/PhysRevResearch.3.043061>.
- [13] M. A. Bates, G. Skačej, C. Zannoni, Defects and ordering in nematic coatings on uniaxial and biaxial colloids, *Soft Matter* 6 (2010) 655–663. doi:<https://doi.org/10.1039/B917180K>.
- [14] M. A. Bates, Computer simulation studies of nematic liquid crystal tactoids, *Chemical physics letters* 368 (2003) 87–93. doi:[https://doi.org/10.1016/S0009-2614\(02\)01824-9](https://doi.org/10.1016/S0009-2614(02)01824-9).
- [15] X. Xing, H. Shin, M. J. Bowick, Z. Yao, L. Jia, M.-H. Li, Morphology of nematic and smectic vesicles, *Proceedings of the National Academy of Sciences* 109 (2012) 5202–5206. doi:[10.1073/pnas.1115684109](https://doi.org/10.1073/pnas.1115684109).
- [16] L. Ding, R. A. Pelcovits, T. R. Powers, Deformation and orientational order of chiral membranes with free edges, *Soft Matter* 17 (2021) 6580–6588. doi:<https://doi.org/10.1039/D1SM00629K>.
- [17] N. B. Ludwig, K. L. Weirich, E. Alster, T. A. Witten, M. L. Gardel, K. Dasbiswas, S. Vaikuntanathan, Nucleation and shape dynamics of model nematic tactoids around adhesive colloids, *The Journal of chemical physics* 152 (2020) 1–12. doi:<https://doi.org/10.1063/1.5141997>.
- [18] L.-Q. Chen, Phase-field models for microstructure evolution, *Annual review of materials research* 32 (2002) 113–140. doi:[10.1146/annurev.matsci.32.112001.132041](https://doi.org/10.1146/annurev.matsci.32.112001.132041).
- [19] P. Cermelli, A. J. D. Scala, Constant-angle surfaces in liquid crystals, *Philosophical Magazine* 87 (2007) 1871–1888. doi:<https://doi.org/10.1080/14786430601110364>.

- [20] F. Gibou, R. Fedkiw, S. Osher, A review of level-set methods and some recent applications, *Journal of Computational Physics* 353 (2018) 82–109. doi:<https://doi.org/10.1016/j.jcp.2017.10.006>.
- [21] I. Nitschke, S. Reuther, A. Voigt, Liquid crystals on deformable surfaces, *Proceedings of the Royal Society A* 476 (2020) 1–23. doi:<https://doi.org/10.1098/rspa.2020.0313>.
- [22] C. D. Schimming, J. Viñals, S. W. Walker, Numerical method for the equilibrium configurations of a maier-saupe bulk potential in a q-tensor model of an anisotropic nematic liquid crystal, *Journal of Computational Physics* 441 (2021) 1–21. doi:<https://doi.org/10.1016/j.jcp.2021.110441>.
- [23] A. DeBenedictis, T. J. Atherton, Shape minimisation problems in liquid crystals, *Liquid Crystals* 43 (2016) 2352–2362. doi:<https://doi.org/10.1080/02678292.2016.1209699>.
- [24] J. H. Adler, T. J. Atherton, D. B. Emerson, S. P. MacLachlan, An energy-minimization finite-element approach for the frank–oseen model of nematic liquid crystals, *SIAM Journal on Numerical Analysis* 53 (2015) 2226–2254. doi:<https://doi.org/10.1137/140956567>.
- [25] J. Nocedal, S. J. Wright, *Numerical optimization*, Springer, 1999.
- [26] C. G. Broyden, J. E. D. Jr, J. J. Moré, On the local and superlinear convergence of quasi-newton methods, *IMA Journal of Applied Mathematics* 12 (1973) 223–245. doi:<https://doi.org/10.1093/imamat/12.3.223>.
- [27] G. Starke, Gauss–newton multilevel methods for least-squares finite element computations of variably saturated subsurface flow, *Computing* 64 (2000) 323–338. doi:[10.1007/s006070070028](https://doi.org/10.1007/s006070070028).
- [28] W. L. Briggs, V. E. Henson, S. F. McCormick, *A multigrid tutorial*, SIAM, 2000.
- [29] U. Trottenberg, C. W. Oosterlee, A. Schuller, *Multigrid*, Elsevier, 2000.
- [30] J. H. Adler, D. B. Emerson, S. P. MacLachlan, T. A. Manteuffel, Constrained optimization for liquid crystal equilibria, *SIAM Journal on*

- Scientific Computing 38 (2016) B50–B76. doi:<https://doi.org/10.1137/141001846>.
- [31] P. E. Farrell, A. Birkišson, S. W. Funke, Deflation techniques for finding distinct solutions of nonlinear partial differential equations, *SIAM Journal on Scientific Computing* 37 (2015) A2026–A2045. doi:<https://doi.org/10.1137/140984798>.
- [32] J. H. Adler, D. B. Emerson, P. E. Farrell, S. P. MacLachlan, Combining deflation and nested iteration for computing multiple solutions of nonlinear variational problems, *SIAM Journal on Scientific Computing* 39 (2017) B29–B52. doi:<https://doi.org/10.1137/16M1058728>.
- [33] D. B. Emerson, P. E. Farrell, J. H. Adler, S. P. MacLachlan, T. J. Atherton, Computing equilibrium states of cholesteric liquid crystals in elliptical channels with deflation algorithms, *Liquid Crystals* 45 (2018) 341–350. doi:<https://doi.org/10.1080/02678292.2017.1365385>.
- [34] J. Xia, S. MacLachlan, T. J. Atherton, P. E. Farrell, Structural landscapes in geometrically frustrated smectics, *Physical Review Letters* 126 (2021) 1–6. doi:[10.1103/PhysRevLett.126.177801](https://doi.org/10.1103/PhysRevLett.126.177801).
- [35] A. Ramage, E. C. G. Jr, A preconditioned nullspace method for liquid crystal director modeling, *SIAM Journal on Scientific Computing* 35 (2013) B226–B247. doi:<https://doi.org/10.1137/120870219>.
- [36] R. H. Nochetto, S. W. Walker, W. Zhang, A finite element method for nematic liquid crystals with variable degree of orientation, *SIAM Journal on Numerical Analysis* 55 (2017) 1357–1386. doi:<https://doi.org/10.1137/15M103844X>.
- [37] C. S. MacDonald, J. A. Mackenzie, A. Ramage, A moving mesh method for modelling defects in nematic liquid crystals, *Journal of Computational Physics: X* 8 (2020) 1–18. doi:<https://doi.org/10.1016/j.jcpx.2020.100065>.
- [38] J. Xia, P. E. Farrell, Variational and numerical analysis of a q-tensor model for smectic-a liquid crystals, *ESAIM: Mathematical Modelling and Numerical Analysis* 57 (2023) 693–716. doi:<https://doi.org/10.48550/arXiv.2110.06479>.

- [39] F. C. Frank, I. liquid crystals. on the theory of liquid crystals, *Discussions of the Faraday Society* 25 (1958) 19–28. doi:<https://doi.org/10.1039/DF9582500019>.
- [40] N. J. Mottram, C. J. P. Newton, Introduction to q-tensor theory, arXiv preprint arXiv:1409.3542 (2014) 1–20doi:<https://doi.org/10.48550/arXiv.1409.3542>.
- [41] M. Nestler, I. Nitschke, A. Voigt, A finite element approach for vector- and tensor-valued surface pdes, *Journal of Computational Physics* 389 (2019) 48–61. doi:<https://doi.org/10.1016/j.jcp.2019.03.006>.
- [42] P. E. Farrell, A. Hamdan, S. P. MacLachlan, Finite-element discretization of the smectic density equation, *IMA Journal of Numerical Analysis* 00 (2023) 1–36. doi:<https://doi.org/10.48550/arXiv.2207.12916>.
- [43] A. E. Diegel, S. W. Walker, A finite element method for a phase field model of nematic liquid crystal droplets, *Commun. Comput. Phys.* 25 (2019) 155–188. doi:[doi:10.4208/cicp.0A-2017-0166](https://doi.org/10.4208/cicp.0A-2017-0166).
- [44] J. P. Borthagaray, R. H. Nochetto, S. W. Walker, A structure-preserving fem for the uniaxially constrained q-tensor model of nematic liquid crystals, *Numerische Mathematik* 145 (2020) 837–881. doi:<https://doi.org/10.1007/s00211-020-01133-z>.
- [45] M. Hirsch, F. Weber, A convergent finite element scheme for the q-tensor model of liquid crystals subjected to an electric field, arXiv preprint arXiv:2307.11229doi:<https://doi.org/10.48550/arXiv.2307.11229>.
- [46] M. Benzi, G. H. Golub, J. Liesen, Numerical solution of saddle point problems, *Acta numerica* 14 (2005) 1–137. doi:<https://doi.org/10.1017/S0962492904000212>.
- [47] F. Bach, R. Jenatton, J. Mairal, G. Obozinski, et al., Convex optimization with sparsity-inducing norms, *Optimization for machine learning* 5 (2011) 19–53.
- [48] C. Joshi, D. Goldstein, C. Wennerholm, E. Downey, E. Hamilton, S. Hocking, A. Andrei, J. H. Adler, T. J. Atherton, Morpho—a programmable environment for shape optimization and shapeshifting

problems, arXiv preprint arXiv:2208.07859doi:<https://doi.org/10.48550/arXiv.2208.07859>.